Journal of Energy Storage 90 (2024) 111929

Contents lists available at ScienceDirect

Journal of Energy Storage

journal homepage: www.elsevier.com/locate/est

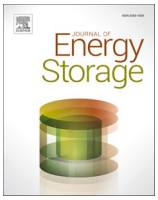

Research Papers

Tubular design and metal ratio refinement of copper telluride electrodes for superior volumetric capacity in potassium-ion batteries

Che-Bin Chang [1], Hsin-Yun Tsai [1], Hsing-Yu Tuan [*]

Department of Chemical Engineering, National Tsing Hua University, Hsinchu 30013, Taiwan

ARTICLE INFO

Keywords:
Copper
Tellurium
Potassium
Energy storage
Anode

ABSTRACT

Despite encountering various challenges in the production of high volumetric capacity potassium-ion batteries (PIBs), metal tellurides present a promising solution owing to their high density and conductivity. In this work, we synthesized copper telluride nanotubes, measuring 2–5 μm in length with a wall thickness of 30 nm, employing a two-step hot injection method as anode materials for high volumetric capacity PIBs. Their electrochemical behavior was investigated via in-situ X-ray diffraction (XRD), elucidating the precipitation of metallic copper during K^+ insertion. Through meticulous adjustment of the copper content, exceptional volumetric capacity (2225.1 mA h cm^{-3}) and impressive rate capacity (994 mA h cm^{-3}) were ultimately attained. Notably, the material exhibited over 150 cycles at a current density of 500 mA h g^{-1} with negligible capacity degradation. This work underscores the significance of the tellurium-to-copper ratio, demonstrating that a 2:1 ratio is pivotal for optimizing tellurium utilization and enhancing electrode rate performance. Moreover, the nanotubes structure substantially augmented the reactive surface area while mitigating issues associated with volume expansion. These discoveries position copper telluride nanotubes as robust contenders for the next generation of high-capacity PIBs anode.

1. Introduction

With the pursuit of carbon neutrality escalating, the demand for green energy economies is on the rise, thereby precipitating a marked increase in the requisite for energy storage technologies. While lithium-ion batteries (LIBs) technology currently hold sway in the market owing to their advantageous high energy and power density properties, apprehensions regarding the disparate distribution and scarcity of lithium resources have mounted. Potassium metal, characterized by a comparable redox potential (−2.93 V vs the standard hydrogen electrode (SHE)) to lithium and abundant reserves in the Earth's crust, emerges as a viable alternative for LIBs [1]. As wearable and smart electronic devices progressively shrink in size, there is a burgeoning emphasis on the high volumetric capacity of secondary batteries, propelling the pursuit of efficient component design and packaging [2–4]. Despite a predominant focus on enhancing the specific capacity of anode materials, there are only few cases targeting high volumetric capacity in PIBs [5,6]. Carbon-based materials, commonly used as negative electrodes, offer a low theoretical volumetric capacity of 628 mA h cm^{-3}, thus consuming a significant portion of battery volume [7–10]. Alloying-type materials like Sb and bismuth Bi present lower operating potentials alongside outstanding specific capacity. Nonetheless, their susceptibility to extreme volume expansion, ranging from 300 % to 400 %, precipitates material fracture and precipitous capacity decline [11–14]. Consequently, identifying high volumetric capacity anode materials for PIBs remains a significant challenge.

Chalcogen elements like sulfur (S), selenium (Se), and tellurium (Te) have gained interest for K^+ storage due to their high theoretical specific capacity and broad applicability [15–17]. Particularly, tellurium stands out for its larger atomic size (1.42 Å), lower electronegativity, and higher electrical conductivity (2×10^2 S m^{-1}) compared to S and Se, both of which have conductivities of 5×10^{-16} S m^{-1} [18–20]. These properties not only enable more space for K^+ but also improve ion dynamics, allowing for high utilization rates and excellent rate performance at elevated current densities [21]. Furthermore, tellurium's high density (6.24 g cm^{-3}) provides an ultra-high volumetric capacity of around 2621 mA h cm^{-3}, compensating for its lower gravimetric capacity (419 mA h g^{-1}) [22,23]. Elemental tellurium's conversion

* Corresponding author.
E-mail address: hytuan@che.nthu.edu.tw (H.-Y. Tuan).
[1] These authors contributed equally to this work.

https://doi.org/10.1016/j.est.2024.111929
Received 7 January 2024; Received in revised form 29 March 2024; Accepted 30 April 2024
Available online 11 May 2024

reactions produce soluble polytellurides (K_2Te_3), causing material loss and metal surface deposition—a problem also seen with sulfur and selenium [24,25]. Liu et al. has essentially established the conversion reaction mechanism for K—Te systems and demonstrated near-theoretical capacitance performance (409 mA h g^{-1}) in initial cycles [26]. Although polytelluride dissolution can be improved in high-concentration (5 M) electrolytes, long-term cycling performance still requires further optimization.

Creating efficient electrode materials remains crucial for enhancing long-term cycling performance. A prevalent method involves embedding tellurium (Te) in a carbon framework through melt diffusion [27,28]. Such a technique alleviates shuttle effects often seen in multi-step conversion processes, thereby increasing reaction areas and enhancing rate performance [29,30]. However, incorporating carbon-based materials does come with drawbacks—specifically, a reduction in electrode volumetric capacity. Another promising route involves using transition metal telluride nanotubes. Adding transition metals may decrease active material proportion but could also boost overall density, depending on the specific metal [31–33]. Maintaining high volumetric capacity becomes possible, albeit with a reduced gravimetric capacity. Additionally, large surface areas and unique tube-like shapes in these nanotubes contribute to improved cycling and rate performance [34,35]. In addition to material development, the battery manufacturing process utilizing electro spraying on the separator is anticipated to further enhance electrochemical performance [36].

This study employs the hot injection method to synthesize copper telluride nanotubes of varying copper content, achieving key performance benchmarks—high volumetric capacity, excellent rate performance, and stable cycling—for K^+ batteries. Incorporating metallic copper into a Te framework boosts material density, with $Cu_{1.46}Te$ displaying a density of 7.53 g cm^{-3}. Despite reducing Te content, copper inclusion improves Te utilization as an active material, mainly through in situ copper precipitation during conversion reactions. Cu_2Te nanotubes display robust volumetric capacity, peaking at 2259 mA h cm^{-3} with a low current density of 50 mA g^{-1}. Remarkably, such volumetric capacity remains high at 994.0 mA h cm^{-3} even with elevated current densities (5000 mA g^{-1}). Efficiency in both material utilization and rate performance originates from high conductivity inherent to Te and from copper formation during conversion reactions. These elements synergistically minimize the shuttle effects occurs in K—Te conversion reaction during K^+ insertion and also decrease the electrode resistance. This study refines tubular design and metal ratios to enhance material efficiency and rate performance in conversion reactions, providing pivotal insights for improving anode materials in PIBs, emphasizing volumetric capacity and prolonged cycle life.

2. Experimental section

2.1. Materials

Tellurium dioxide (TeO_2, 99 + %), Ethylene glycol (EG, 99 + %) and potassium chunk were purchased by Acros organics. Polyvinylpyrrolidone (PVP, Mw ~ 40,000), ascorbic acid (Vitamin C), copper nitrate hemipentahydrate ($Cu(NO_3)_2{\cdot}2.5H_2O$), carboxymethyl cellulose (NaCMC, Mw ~ 700,000), methoxymethane (DME, anhydrous, ≥99 %), hexadecyl trimethyl ammonium bromide (CTAB, 99 %), potassium chloride (KCl, ≥99 %), potassium hexacyanoferrate(II) trihydrate ($K_4Fe(CN)_6{\cdot}3H_2O$, ≥98.5 %), Potassium hydroxide (KOH, extra pure grade) was purchased by Duksan Techopia. Potassium bis(fluorosulfonyl)imide (KFSI, 97 %) was purchased from Combi-Blocks. Super-P was purchased from shining energy. CR-2032 coin-type cell was purchased by JuChen company. 10 μm of Cu foil and Al foil were purchased by Chang Chun Group. Glass fiber was purchased by Advantec.

2.2. Synthesis of copper telluride (x = 2.0, 1.5, 1.0, 0.5) nanotubes

In a typical procedure, 0.167 g of TeO_2, 0.167 g of KOH, and 0.1 g of PVP were added into a 50 mL three-neck flask. Then, 15 mL of EG was injected and the reaction mixture formed a homogeneous transparent solution under vigorous stirring. The mixture solution was heated to 140 °C with a rate of 2 °C min^{-1}. When the temperature of solution reached 140 °C, 0.75 mL distilled water contain 0.25 g of ascorbic acid was injected. After the solution was kept at 130 °C for 1 h, the temperature was raised to 160 °C and 0.465 g of $Cu(NO_3)_2{\cdot}2.5H_2O$ (ca. 2 mmol) dissolved in 3 mL of EG was injected. The flask was maintained at 160 °C for 1 h and then cooled to room temperature naturally. The obtained gray solids were collected by centrifuging the reaction mixture; the particles were then washed with deionized (DI) water once and the solution with the ratio of DI water and ethanol 1:1 twice. Then the particles were dried with rotary evaporator before further characterization. Other ratios of copper telluride nanotubes were prepared by adding different amount of $Cu(NO_3)_2{\cdot}2.5H_2O$ or PVP in the same procedure.

2.3. Synthesis of Cu_7Te_4 nanowires

Typically, the 0.5 mmol TeO_2, 0.5 mmol KOH, 0.1 of cetyltrimethylammonium bromide (CTAB) and 1.0 of ascorbic acid were added in 40 mL of DI water. Then, ramp the temperature to 90 °C with the rate of 2 °C min^{-1} with vigorous stirring for 1 h. After 1 h, the solution become opaque gray color, indicating the Cu_7Te_4 nanowires formation. The as-synthesized nanowires were collected by centrifugation and wash by ethanol and DI water (v% 1:1) three times. Finally, dry the residue solvent with rotary evaporator, the Cu_7Te_4 nanowires power was obtained.

2.4. Synthesis of Prussian blue nanoparticles

Prussian blue nanoparticles were synthesis via typical co-precipitation method modified from the previous paper [37]. First, 5 mmol of $K_4Fe(CN)_6{\cdot}3H_2O$ and 20 g of KCl were dissolved in 100 mL deionized water with vigorous stirring denoted as solution A. Second, 3 mmol of $FeCl_2$ was dissolved in 100 mL deionized water denoted as solution B. Then, solution B was dropwise added in solution A by syringe pump with the flow rate of 25 mL hr^{-1}, upon solution B added, the dark blue precipitation will form immediately. After solution B drop in all, Prussian blue nanoparticles were collected by centrifugation with 8000 rpm for 5 mins and further wash by ethanol and DI water (1:1 v%) with 8000 rpm for 5 mins to remove redundant KCl.

2.5. Material characterization

All materials were drop on silicon wafer and until solvent evaporate, further characterized by using scanning electron microscopy (SEM, HITACHI-SU8010) with 10 kV accelerating voltage, X-ray diffraction (XRD, Bruker D8 ADVANCE). XPS spectra was collected by X-ray photoelectron spectroscopy (XPS, ULVAC-PHI, PHI Quantera II). HRTEM images were obtained by transmission electron microscopy (TEM, JEOL, JEM-ARM200FTH). Surface area was determined by Specific Surface Area and Porosimetry Analyzer (ASAP 2020, Micromeritics).

2.6. Electrochemical measurement

Potassium-ion half cells were prepared by mixing active material (copper telluride, 70 wt%), conductive agent (Super-P, 20 wt%) and binder (NaCMC, 10 wt%) to a homogeneous slurry. After that, coating on copper current collector by a doctor blade and dried in vacuum at 80 °C for 1 h, further cut in a 12 mm circular electrode. The active material loading was at a range of 0.9–1.2 mg cm^{-2}, which measured

with 0.1 μg resolution electronic balance (Sartorius SE2). The electrolyte for half cell was 4 M KFSI in DME, counter electrode was homemade potassium foil and glass fiber as separator. The coin cells assembly were performed in an argon-filled glove box with low oxygen (O_2 < 0.1 ppm) and moisture (H_2O < 0.1 ppm) condition (M. Braun UNILAB). Galvanostatic discharge/charge curves were collected by Neware CT-4000 galvanostat. The GITT test was performed on Maccor series 4000 galvanostat at the current density of 50 mA g^{-1} and 1 h relaxation time. For the PBNPs electrode preparation, active material (PBNPs, 70 wt%), conductive agent (MWCNT, 20 wt%) and binder (NaCMC 10 wt%) were well-mixed to form a uniform slurry, then coated on the Al foil and dried in vacuum at 80 °C for 1 h. Before the full-cells assembly, both anode and cathode were activated by 3 cycles at low current density. The working window of half and full cells were 0.01–3.00 V and 1.00–3.80 V, respectively. The active material ratio of anode/cathode was set as 1:4. The volumetric capacities of copper telluride nanotubes with varying copper contents, except for Cu_7Te_4 nanowires and Te nanotubes, were calculated based on a density of 7.53 g cm^{-3}. This was derived from the results obtained from XRD diffraction patterns.

3. Result and discussion

Shape-defined copper telluride nanotubes were synthesized in two primary steps: the creation of a Te nanotubes template through hot injection and a subsequent cation exchange reaction with variable Cu^{2+} doses (as depicted in Fig. 1). Uniform Te nanotubes results from dissolving TeO_2, KOH, and PVP in EG at 130 °C, forming a transparent yellow TeO_3^{2-} solution. Rapid injection of ascorbic acid reduces the solution into a colloidal metallic Te mixture. During reduction, Te seed crystals undergo recrystallization, leading to hollow nanotubes (as shown in Fig. S1). PVP's controlling role contributes to this unique structure [38]. Experiments with varying PVP amounts clarifies its influence on Te nanotubes synthesis. Low-magnification SEM images (Fig. S2a–c) reveal more micron-sized agglomerates in control samples with less PVP, indicating uncontrolled Te nanocrystal growth. High-magnification SEM images (Fig. S2d–f) confirm increased nanotubes production with added PVP, underlining its importance in controlling nanotubes shape. Importantly, pristine Te nanotubes templates were synthesized without noxious hydrazine, using safer ascorbic acid instead. In subsequent alloying reactions, varying amounts of $Cu(NO_3)_2$ introduce different Cu concentrations, resulting in copper telluride nanotubes with variable properties.

To elucidate the product's surface morphology, we utilized SEM and TEM. Fig. 2a. displays the synthesized copper telluride nanotubes with a curved, uniform morphology, measuring 2–5 μm in length. The high-magnification SEM image (Fig. 2b) reveals a wall thickness of 30 nm and a diameter of 70–100 nm. Compared to the single element Te nanotubes, the wall thickness of Cu_2Te nanotubes has increased and is slightly curved, indicating copper metal's alloying reaction. TEM image (Fig. 2c) shows a 2 μm-long Cu_2Te nanotubes, aligning with the SEM image. The detailed view in Fig. 2d reveals a hollow structure with surface nanoparticles, confirming the template-engaged topotactic reaction. The enlarged TEM (Fig. 2e) reveals similar tube thickness and diameter as the SEM, along with clear bending. HRTEM (Fig. 2f) depicts the crystallinity of Cu_2Te nanotubes with 0.21 nm crystals linked to the (112) plane of $Cu_{1.46}Te$. Additionally, the central HRTEM view (Fig. 2g) presents lattice stripes at 0.21 nm and 0.33 nm, aligning with the (112) and (101) crystal planes, respectively. The FFT image (Fig. 2h) displays distinct diffraction patterns aligned with the crystal planes identified by HRTEM. To determine the distribution of Cu and Te within the nanotubes, we conducted energy dispersive X-ray spectroscopy (EDS). Figure i show high-angle annular dark-field (HAADF) images of Cu_2Te nanotubes, complemented by their respective EDS elemental distribution visuals. The hollow tubular morphology is more discernible in the

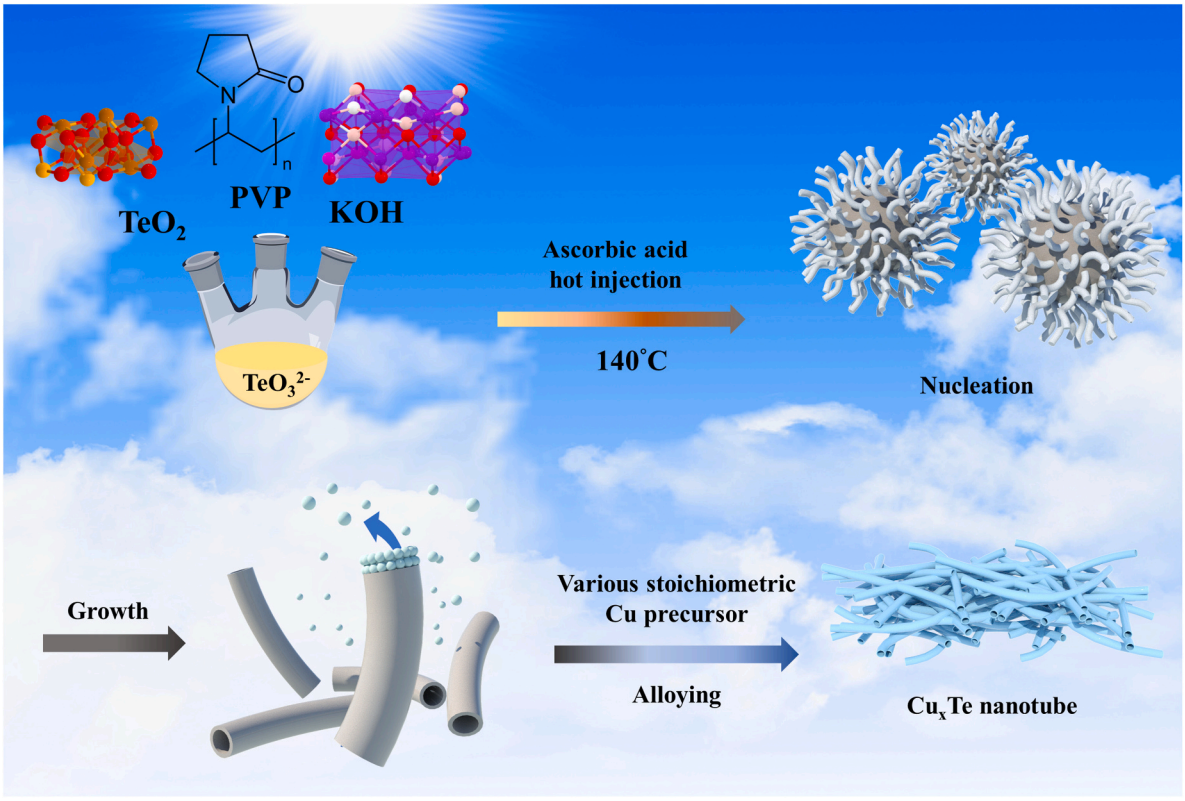

Fig. 1. Schematic representation of the synthesis process for Cu_2Te nanotubes. Starting from TeO_2 molecules in the presence of PVP and KOH, a hot injection of ascorbic acid at 140 °C promotes nucleation. Subsequent growth and alloying phases, involving various stoichiometric Cu precursors, inducing in the formation of Cu_2Te nanotubes. The process highlights critical stages including molecular interaction, nucleation, growth, and alloying to yield the desired nanotubes structure.

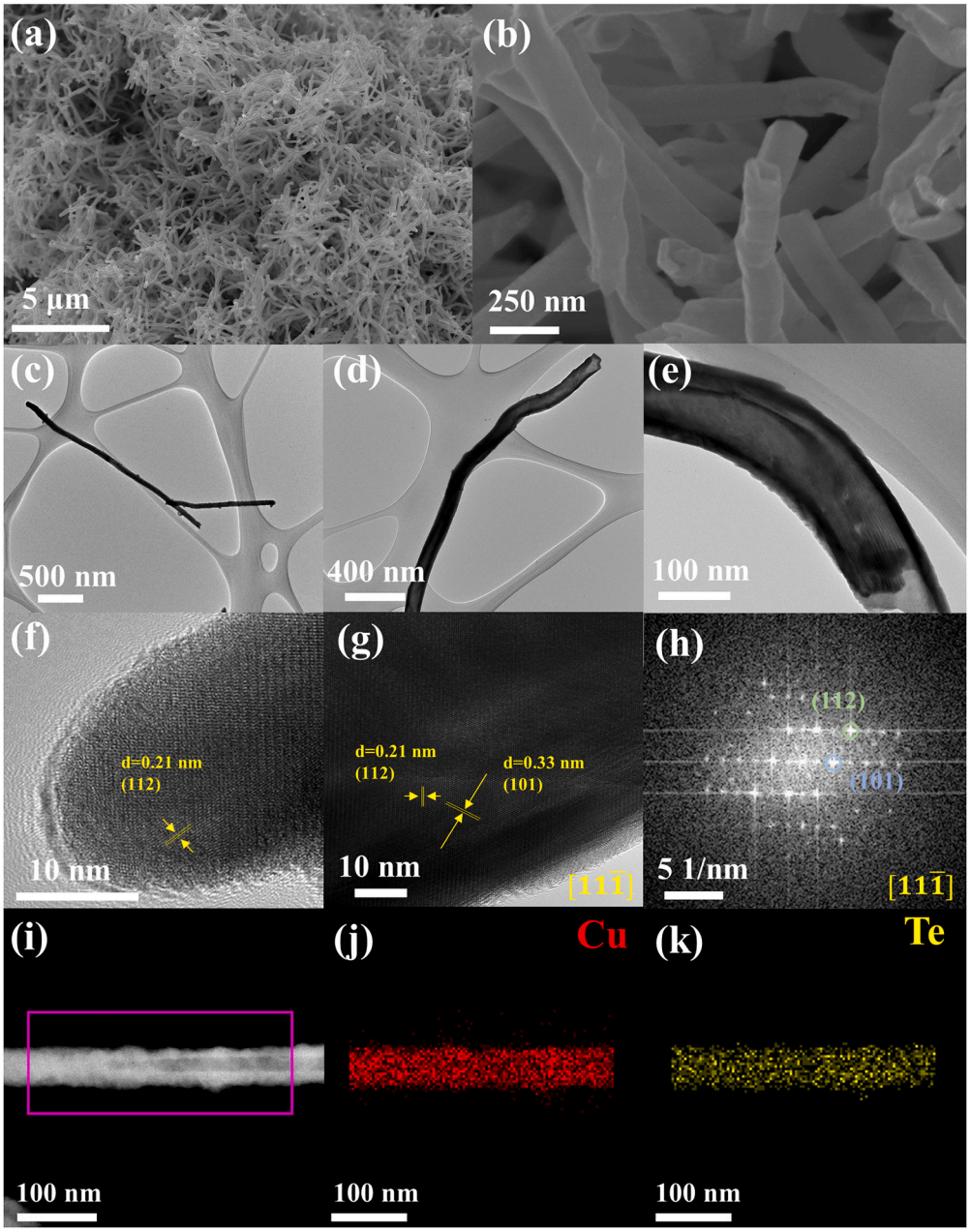

Fig. 2. Morphology characterization of Cu_2Te nanotubes. (a) Low magnification SEM image of Cu_2Te nanotubes. (b) Cross-sectional SEM image of Cu_2Te nanotubes (c) Low magnification TEM image of Cu_2Te nanotubes. (d) TEM images of the tubular structure of Cu_2Te. (e) TEM image showing the wall thickness and diameter of Cu_2Te nanotubes. HRTEM image of Cu_2Te nanotubes from (f) the end of the tube and (g) top of the tube. (h) Corresponding FFT pattern from HRTEM image. (i) HAADF image of Cu_2Te nanotubes and corresponding EDS mapping of (j) Cu and (k) Te in Cu_2Te nanotubes.

dark field images. Elemental distribution analysis of Cu and Te (Figure j, k) indicates a uniform distribution across the nanotubes. Furthermore, based on the results from the energy dispersive spectroscopy, the atomic ratio of Cu to Te approximates the anticipated 2:1 ratio (Fig. S3).

The XRD analysis of Cu_2Te nanotubes is presented in Fig. 3a, revealing an orthorhombic crystal structure. Distinct diffraction peaks are evident at 26.7°, 31.7°, 35.0°, 43.6°, and 45.6°. These peaks correspond to the (101), (110), (111), (112), and (200) crystal planes, respectively. This alignment is consistent with $Cu_{1.46}Te$ (PDF#04–010-3165) in the Pnma space group. The derived lattice parameters are 3.9727 Å (a), 4.0020 Å (b), and 6.1066 Å (c). In addition, the XRD pattern of template intrinsic Te and different copper ratio nanotubes were shown in Figs. S4–S5. To verify the copper ratio in control sample, EDS spectrums were also conducted in Fig. S6. To better ascertain the absolute proportion of copper elements, Inductively Coupled Plasma (ICP) testing was conducted (Fig. S7). Apart from a slightly higher copper content in $Cu_{2.0}Te$, the copper elemental content ratios in various copper telluride nanotubes align with the results obtained from EDS measurements. Different amounts of $Cu(NO_3)_2$ added result in various copper ratios in copper telluride nanotubes. There are three copper ratios of copper telluride nanotubes denoted as $Cu_{0.5}Te$, $Cu_{1.0}Te$, and $Cu_{1.5}Te$, respectively. These designations represent the actual copper and tellurium ratio in the nanotubes. In Fig. 3b, the isothermal adsorption and desorption curves of Cu_2Te nanotubes, obtained using the BET method with nitrogen as the adsorbate, display a specific surface area of 15.03 $m^2\ g^{-1}$. The isothermal adsorption and desorption curves of nanotubes with different copper ratios exhibit a similar surface area to that of Cu_2Te nanotubes (Fig. S8). Additionally, the pore size

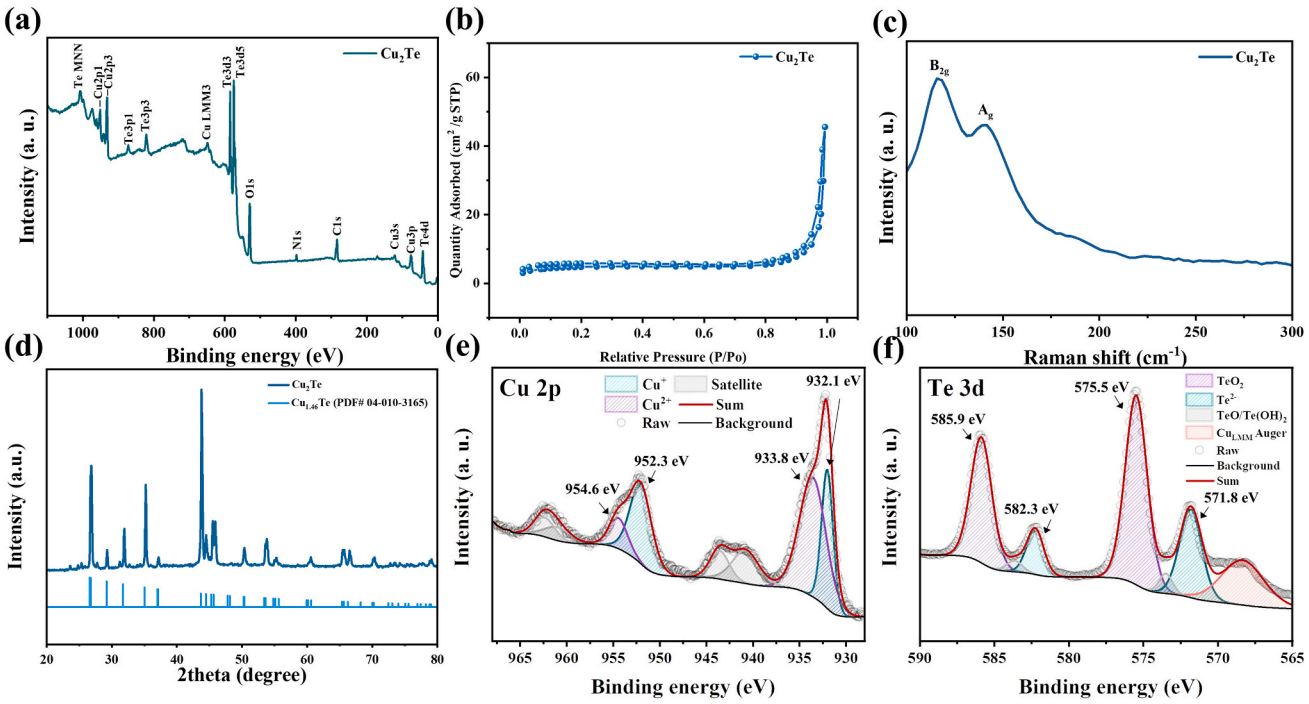

Fig. 3. Structure characterization of Cu_2Te nanotubes. (a) XRD pattern of Cu_2Te nanotubes. (b) Nitrogen adsorption-desorption isotherms curve of Cu_2Te nanotubes (c) Raman spectrum of the Cu_2Te nanotubes. (d) XPS survey scan of Cu_2Te nanotubes. High resolution XPS spectrum of (e) Cu 2p region and (f) Te 3d region of the Cu_2Te nanotubes.

distribution of Cu_2Te nanotubes is in the range of 60–80 nm (Fig. S9). This notable surface area is ascribed to the expansive specific surface offered by the hollow tubular architecture [39]. The Raman spectrum for Cu_2Te nanotubes (Fig. 3c) features pronounced Raman bands at 116 cm^{-1} and 142 cm^{-1}, which are derived from the inherent Raman characteristics of the Te element [40]. Elemental and valence state analysis of the synthesized nanotubes was conducted using XPS. Fig. 3d provides a comprehensive spectral survey of the nanotube components. Prominent peaks corresponding to Cu and Te elements are evident, verifying their presence in the nanotubes. In the detailed Cu 2p spectrum (Fig. 3e), distinct peaks at 952.3 eV and 932.1 eV can be identified, which are consistent with the Cu $2p_{1/2}$ and Cu $2p_{3/2}$ states, respectively, characteristic of Cu(I) chalcogenides [41]. Through XPS analysis, peaks at 954.6 eV and 933.8 eV are identified, corresponding to Cu(II) species, indicative of partial surface oxidation. In the high-resolution Te 3d spectrum (Fig. 3f), peaks at 585.9 eV and 575.5 eV are observed, attributed to TeO_2, resulting from surface oxidation [42]. The presence of Te $3d_{3/2}$ and Te $3d_{5/2}$ peaks at 582.3 eV and 571.8 eV, respectively, align with the expected values for the Te^{2-} reduction state, confirming the Te element's 2^- valence state in the nanotubes [43]. These detailed XPS spectra of Cu and Te validate the successful synthesis of Cu_2Te nanotubes.

The K^+ storage capacity of copper telluride nanotubes was tested using potassium metal foil as the counter electrode in CR2032 coin cells, with a voltage range of 0.01–3.00 V. To assess the effect of copper content and on performance, nanotubes synthesized with varying copper precursor amounts were evaluated. Besides, nanowire structure characterization of Cu_7Te_4 material was also conducted (Figs. S10–S11). Fig. 4a displays the cycling test for four copper telluride nanotubes with different copper levels at a low current density. To better distinguish the electrochemical performance of materials with different copper contents and morphologies, only the discharge capacity has been retained in the plots of capacity versus cycle number. The corresponding Coulombic efficiency data will be provided in the supplementary materials (Fig. S12). During the initial cycles, the stability of the SEI layer and conversion reaction has not yet been established, resulting in initial capacity loss. Notably, during the first 5 cycles, $Cu_{0.5}Te$, $Cu_{1.0}Te$, and $Cu_{1.5}Te$ nanotubes all exhibited a reversible specific capacity of around 300 mA h g^{-1} (2259 mA h cm^{-3}). Copper telluride nanotubes with 0.5 mmol copper content exhibited a reversible specific capacity of around 150 mA h g^{-1}. This lower capacity is likely due to insufficient copper to fully activate the K—Te transformation reaction. In later cycles, Cu_2Te showed a reversible volumetric capacity close to 2288 mA h cm^{-3}. Notably, as copper content rises, the capacity of copper telluride nanotubes also increases, indicating enhanced electrochemical performance with higher copper content. Fig. 4b displays the charge-discharge curves of Cu_2Te nanotubes electrodes at varying current densities. The first discharge curve for the Cu_2Te nanotubes electrode indicates an irreversible capacity, likely due to the formation of a solid electrolyte interface (SEI) layer [44]. In later discharges, two distinct plateaus appear at 1.0 and 0.56 V, aligning with the multi-step conversion reaction of K—Te. A plateau appeared at 1.5 V during charging, consistent with results from Liu et al., which supports the K—Te redox reaction [26]. At a 50 mA g^{-1} current density, the second and third GCD curves are nearly identical, underscoring the stable redox reaction of Cu_2Te nanotubes. The gradual increase of capacity across cycles may stem from SEI layer reformation and material reactivation amidst shifting current densities. Fig. 4c presents electrochemical tests of copper telluride nanotubes at varying copper ratios and current densities. Cu_2Te nanotubes electrode in potassium ion half-cells offer capacity ranging from 994.0 to 2225.1 mA h cm^{-3} (or 132.0 to 295.5 mA h g^{-1}) across current densities from 50 to 5000 mA g^{-1}. Notably, most capacity are consistent at low current densities, with $Cu_{0.5}Te$ being an exception. However, as the current density rises, nanotubes with more copper exhibit slower capacity reduction, likely due to copper precipitation during the reaction. When the current density reverts to 50 mA g^{-1}, the capacity closely mirrors the initial amount, highlighting the electrode structure's stability. The consistent CE across various rates shows that the Cu_2Te nanotubes electrode offers stable and reversible K^+ storage. Furthermore, electrochemical impedance spectroscopy (EIS) spectra were obtained for varying copper contents (Fig. S13). It is noteworthy that the radius of the semicircle in the high-frequency region diminishes with escalating

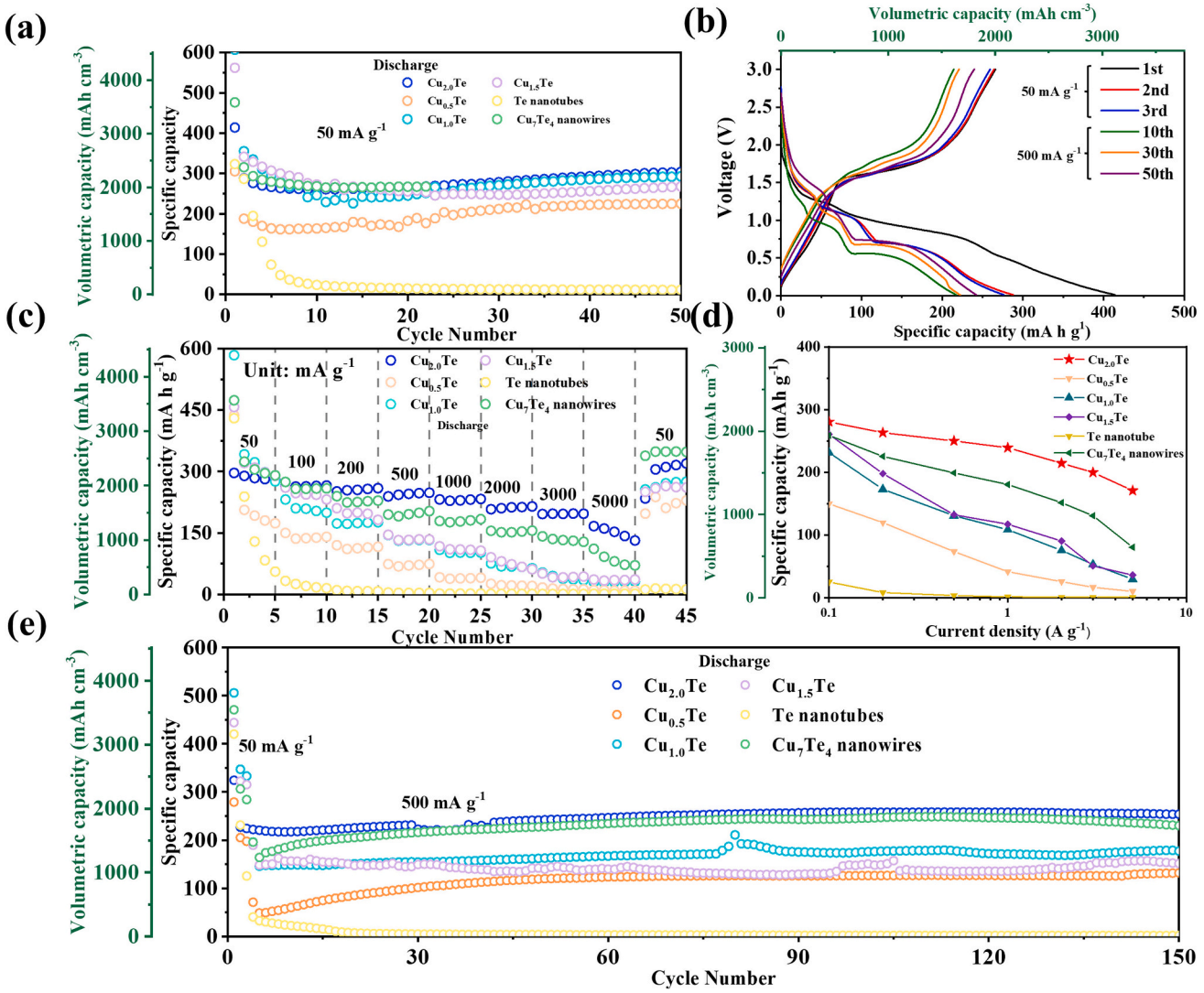

Fig. 4. Potassium ion storage performance of different ratio copper telluride nanotubes. (a) cycling performance and (b) corresponding charge/discharge potential profile of Cu_2Te nanotubes. (c) Rate capability of different ratio copper telluride nanotubes at different current density from 50 to 5000 mA g^{-1}. (d) Summary of reversible discharge capacity of different ratio copper telluride nanotubes at different current density. (e) Cycling performances of different ratio copper telluride nanotubes.

copper content, signifying an augmented interface interaction and charge transfer capability between the nanotubes and the electrolyte. Fig. 4d plots the specific capacity of copper telluride nanotubes electrodes across varying copper ratios and current densities. It highlights that copper ratio significantly influences the high-rate performance of these electrodes due to enhanced conductivity from increased copper precipitation. Even at 5000 mA g^{-1}, the electrode retains a notable capacity of 994.0 mA h cm^{-3} (132.0 mA h g^{-1}). In order to understand the role of copper in the potassiation process, in-situ XRD was performed on Cu_2Te nanotubes, which showed a diffraction peak of metallic copper (Fig. S14). The diffraction peak of metallic copper in the potassiation state suggests the reason for the satisfactory rate performance of Cu_2Te nanotubes. However, the inherent weak crystallinity of polytellurides remains elusive to detection via in-situ XRD. Therefore, ex-situ TEM was employed to scrutinize Cu_2Te nanotubes discharged to 0.01 V (Fig. S15). It was discerned that after fully potassiation, the surface of Cu_2Te nanotubes exhibited roughness, characterized by stacked small particles, yet devoid of discernible fractures (Fig. S15a). Fig. S16 indicated that these small particles corresponded to the (111) crystal planes of metallic Cu and the (200) crystal planes of K_2Te, elucidating the discharge product's composition. Fig. S16a presents the HAADF image of Cu_2Te nanotubes discharged to 0.01 V, manifesting that the nanotubes morphology remains unaltered following potassiation, as observed in the dark-field image. Subsequently, EDS mapping images (Fig. S16b) unveil the homogeneous distribution of Cu, Te, and K elements within the nanotubes, affirming the thorough potassiation of the Cu_2Te nanotubes. Based on the GCD curve, CV curve and in-situ XRD result show similar shape and plateau as LIB, we summarize the possible reaction mechanisms as follows [41]:.

$$Cu_2Te + 2K^+ + 2e^- \leftrightarrow Cu + K_2Te$$

To elucidate the stability of these electrodes across different copper ratios, extended cycling capability tests were undertaken, as depicted in Fig. 4e. After undergoing three activation cycles at a current density of 50 mA g^{-1}, the Cu_2Te nanotubes electrode exhibited negligible capacity loss post 150 cycles, preserving a robust reversible specific capacitance of 1910.4 mA h cm^{-3} (253.7 mA h g^{-1}). The hollow morphology of nanotubes increases surface area for better electrolyte contact, while its copper ratio enhances conductivity, providing stability and resilience to intensive electrochemical cycling for the Cu_2Te nanotubes electrode.

To investigate the performance of Cu_2Te nanotubes electrode, kinetics was analyzed using Cyclic Voltammetry (CV). Fig. 5a shows

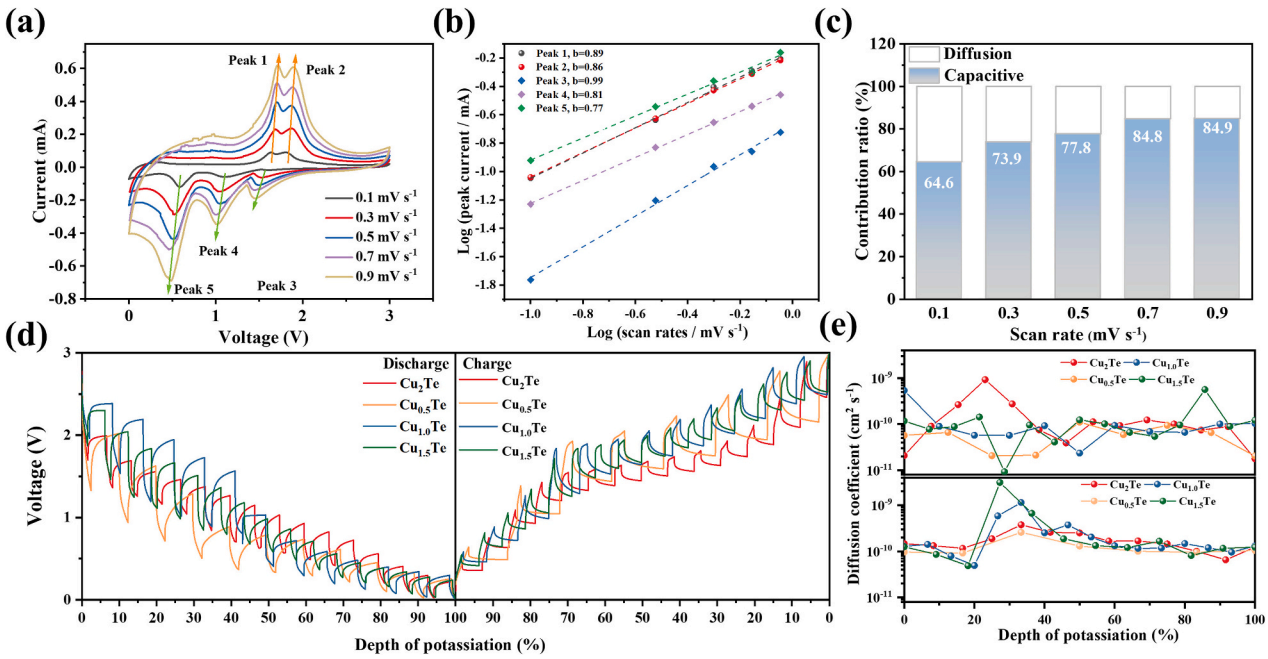

Fig. 5. Kinetic analysis of Cu_2Te nanotubes. (a) CV curve of Cu_2Te nanotubes at various scan rate. (b) b value calculated by fitting log(peak current) and log(various scan rate) from various CV scan rate of Cu_2Te nanotubes. (c) Calculated capacitive contribution of copper telluride nanotubes with various copper content. (d) GITT curve and (e) calculated diffusion coefficient of copper telluride nanotubes with various copper content.

minimal polarization as scan rate increases. The capacitance contribution is derived from the power law relationship between peak current and scan rate [45]:.

$$i = av^b$$

Constants a and b are determined by plotting $log(i)$ against $log(v)$, with i representing peak current and v the scan rate. Typically, b ranges from 0.5 (diffusion controlled) to 1 (surface pseudocapacitance controlled). As shown in Fig. 5b, the b values for various peaks suggest the Cu_2Te nanotubes electrode stores potassium [46].

In the context of the ionic process, it is predominantly governed by a pseudocapacitive mechanism. This swift non-Faradaic process augments the rate performance, elucidating the underlying rationale for the observed superior high-rate performance. Furthermore, the formula detailing the capacitive contribution is delineated below [47]:

$$i(v) = k_1 v + k_2 v^{\frac{1}{2}}$$

Among them, $i(v)$ is the current value at a specific voltage, $k_1 v$ and $k_2 v^{\frac{1}{2}}$ denote the contributions from pseudocapacitance and diffusion, respectively. It is possible to compute the proportion of pseudocapacitive contribution quantitatively. As depicted in Fig. 5c, the pseudocapacitive contributions of the Cu_2Te nanotubes electrode at scan rates of 0.1, 0.3, 0.5, 0.7, and 0.9 mV s^{-1} amount to 64.6 %, 73.9 %, 77.8 %, 84.8 %, and 84.9 %, respectively. The proportion of capacitance contribution exhibits variation as the scan rate incrementally ascends. The Galvanostatic Intermittent Titration Technique (GITT) was employed to determine the K^+ diffusion coefficient (D_{K^+}) for the Cu_2Te nanotubes electrode. Prior to this measurement, three cycles at low current density were executed to mitigate any potential effects from irreversible reactions. The diffusion coefficient D_{K^+} is extrapolated using Fick's second law, delineated as follows [48]:

$$D_{K^+} = \frac{4L^2}{\pi\tau}\left(\frac{m_B V_m}{S M_B}\right)^2 \left(\frac{\Delta E_S}{\Delta E_t}\right)^2$$

Fig. 5d shows the GITT curve of the Cu_2Te nanotubes electrode, and the D_{K^+} of each potassiation state can be calculated. As shown in Fig. 5e, the calculated D_{K^+} of the Cu_2Te nanotubes electrode is between 10^{-9} and 10^{-11} cm^2 s^{-1}, due to the sufficiently large surface area and pseudocapacitive behavior of the nanotubes structure. So that D_{K^+} increases as the state of potassiation increases. Then, due to the accumulation of K^+ that preferentially occupies the active reaction site, it slows down and finally reaches a constant value after the degree of potassiation reaches 23 %. During the process of depotassiation, the value of D_{K^+} did not fluctuate significantly, showing constant depotassiation behavior.

Inspired by the strong electrochemical performance of half cell, a coin-type full cell was assembled using PB as the positive electrode and Cu_2Te nanotubes as the negative. The same electrolyte of half cell was used, as depicted in Fig. 6a. PB, made using a standard co-precipitation method, has uniformly-sized nanoparticles and XRD pattern (Fig. S17) is consistent with the face-centered cubic $Fe_4[Fe(CN)_6]_3$ (JCPDS-52–1907). From the GCD curves in Fig. 6b, there's a clear capacity difference between the Cu_2Te nanotubes and PB electrodes. Thus, the negative-to-positive electrode material ratio is set at 1:4 for full negative electrode use. Fig. 6c displays the GCD curves of the Cu_2Te//PB full cell at varied current densities, maintaining a stable curve even with rising current, indicating robust rate performance. Fig. 6d indicates the Cu_2Te//PB has reversible discharge capacities of 1373.1, 1264.3, 1108.4, 930.0, and 713.8 mA h cm^{-3} at 200, 300, 500, 1000, and 2000 mA g^{-1} current densities, respectively. Notably, when transitioning from high to low current density, the discharge capacity recovers well, demonstrating the stable redox reaction of the Cu_2Te//PB battery. Fig. 6e indicates the Cu_2Te//PB achieves a peak energy density of 119.4 Wh kg^{-1} and power density of 6881.8 W kg^{-1}. In cycling performance tests, the Cu_2Te//PB retained 810.2 mA h cm^{-3} after 600 cycles at 500 mA g^{-1}, with an 82 % capacity retention, highlighting the potential of Cu_2Te nanotubes electrodes.

Fig. 7 summaries the advantage of Cu_2Te nanotubes. Cu_2Te nanotubes possess high density, which compensates for the capacity occupied by the transition metal in the active material Te, achieving a volumetric capacity similar to that of pristine Te. The tubular design further enhances the specific surface area, increasing the contact area with the electrolyte, implying superior rate capability, and maintaining excellent mechanical strength. Furthermore, the precipitation of copper metal

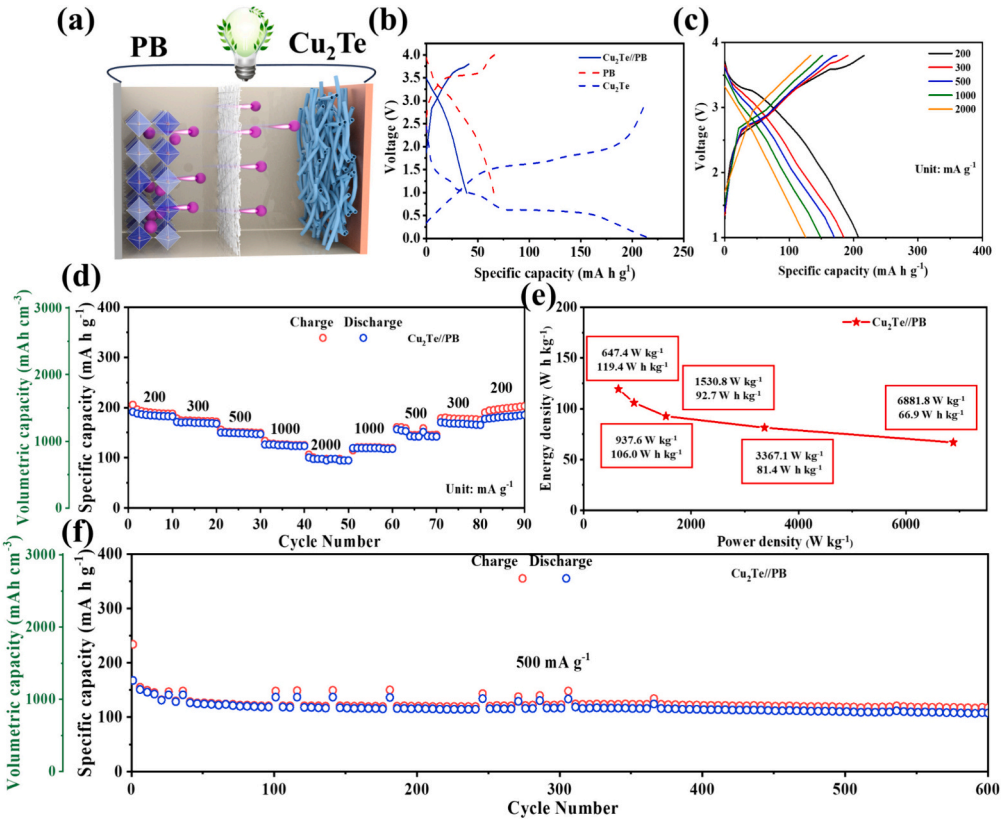

Fig. 6. Electrochemical performance of Cu_2Te//PB full cell. (a) Schematically illustrate the working principle of Cu_2Te//PB full cell. (b) Charge/discharge curve of PB cathode, Cu_2Te anode and Cu_2Te//PB full cell. (c) Charge/discharge profile, (d) rate capability, (e) Ragone plot and (f) cycling performance of Cu_2Te//PB full cell.

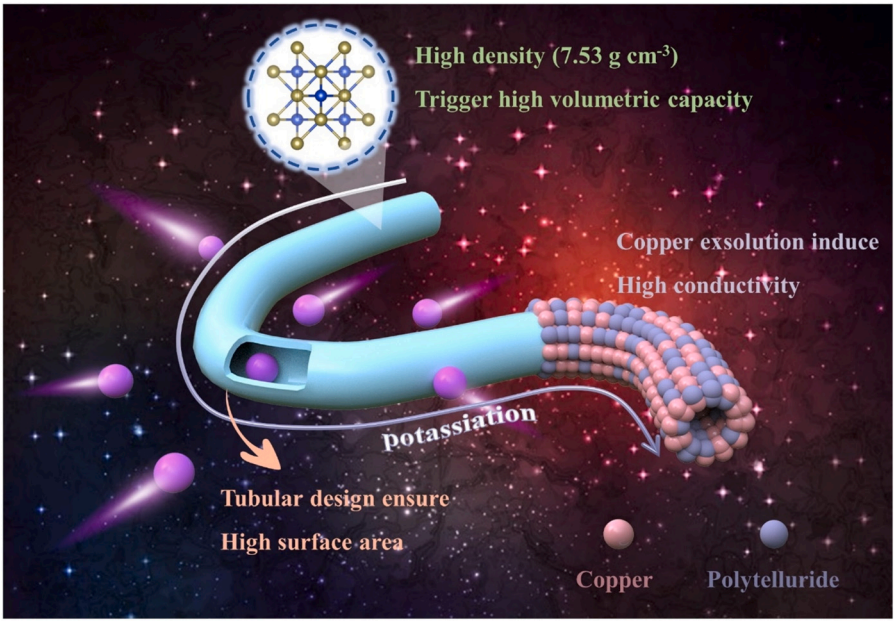

Fig. 7. Schematic illustration the properties of Cu_2Te nanotubes: a high-density configuration enhances volumetric capacity, while the tubular design boosts surface area for efficient potassiation. Copper exsolution augments conductivity, with integration between the tube and constituents like copper and polytelluride emphasizing improved electrochemical performance.

during the K^+ insertion process undoubtedly enhances the overall electrode conductivity, facilitating the kinetics of K^+ diffusion. We believe these factors contribute to the excellent electrochemical performance exhibited by Cu_2Te nanotubes.

4. Conclusion

We synthesized copper telluride nanotubes with different copper ratios as anode materials for PIBs. The nanotubes offer increased electrolyte contact and potassium ion reaction sites due to their vast surface

area. The electrode's performance is markedly influenced by copper precipitation during electrochemical processes. The Cu_2Te nanotubes electrode, with its high copper ratio, demonstrates superior capacity (2259 mA h cm^{-3}), stability over 150 cycles, and robust rate performance (994 mA h cm^{-3} at 5000 mA g^{-1}), thanks to the copper's enhanced conductivity and K—Te conversion kinetics. This structure efficiently handles volume expansion from K^+ storage. Impressively, the Cu_2Te//PB battery showcases remarkable energy (119.4 Wh kg^{-1}) and power densities (6881.8 W kg^{-1}), underscoring its real-world application prospects. The findings highlight the potential of metal telluride as a promising PIBs anode, paving the way for improving the volumetric capacity of such batteries.

CRediT authorship contribution statement

Che-Bin Chang: Writing – original draft, Data curation. **Hsin-Yun Tsai:** Investigation, Data Curation.**Hsing-Yu Tuan:** Writing – original draft, Supervision, Conceptualization.

Declaration of competing interest

The authors declare that they have no known competing financial interests or personal relationships that could have appeared to influence the work reported in this paper.

Data availability

No data was used for the research described in the article.

Acknowledgment

This work received financial support from the 2030 Cross-Generation Young Scholars Program by National Science and Technology Council, Taiwan (NSTC 112-2628-E-007-010 & NSTC 112-2628-E-007-016). The authors thank Mr. Yung-Sheng Chen (Instrumentation center at NTHU) for Spherical-aberration Corrected Field Emission TEM analysis.

Appendix A. Supplementary data

Supplementary data to this article can be found online at https://doi.org/10.1016/j.est.2024.111929.

References

[1] K. Sada, J. Darga, A. Manthiram, Challenges and prospects of sodium-ion and potassium-ion batteries for mass production, Adv. Energy Mater. 13 (39) (2023) 2302321.
[2] M. Fichtner, K. Edström, E. Ayerbe, M. Berecibar, A. Bhowmik, I.E. Castelli, S. Clark, R. Dominko, M. Erakca, A.A. Franco, Rechargeable batteries of the future—the state of the art from a BATTERY 2030+ perspective, Adv. Energy Mater. 12 (17) (2022) 2102904.
[3] L. Mauler, F. Duffner, W.G. Zeier, J. Leker, Battery cost forecasting: a review of methods and results with an outlook to 2050, Energy Environ. Sci. 14 (9) (2021) 4712–4739.
[4] Y. Wang, J. Tian, Z. Sun, L. Wang, R. Xu, M. Li, Z. Chen, A comprehensive review of battery modeling and state estimation approaches for advanced battery management systems, Renew. Sust. Energ. Rev. 131 (2020) 110015.
[5] Z. Zhang, B. Jia, L. Liu, Y. Zhao, H. Wu, M. Qin, K. Han, W.A. Wang, K. Xi, L. Zhang, Hollow multihole carbon bowls: a stress–release structure design for high-stability and high-volumetric-capacity potassium-ion batteries, ACS Nano 13 (10) (2019) 11363–11371.
[6] X. Chang, N. Sun, G. Li, B. Yang, R.A. Soomro, B. Xu, Capillary evaporation-induced fabrication of compact flake graphite anode with high volumetric performance for potassium ion batteries, Adv. Mater. Interfaces 10 (6) (2023) 2201940.
[7] Y.T. Liu, D.D. Han, L. Wang, G.R. Li, S. Liu, X.P. Gao, $NiCo_2O_4$ nanofibers as carbon-free sulfur immobilizer to fabricate sulfur-based composite with high volumetric capacity for lithium–sulfur battery, Adv. Energy Mater. 9 (11) (2019) 1803477.
[8] F. Xin, M.S. Whittingham, Challenges and development of tin-based anode with high volumetric capacity for Li-ion batteries, Electrochem. Energy Rev. 3 (2020) 643–655.
[9] Y.Y. Hsieh, H.Y. Tuan, Oxygen vacancy-tailored Schottky heterojunction activates interface dipole amplification and carrier inversion for high-performance potassium-ion batteries, Small 19 (2023) 2305342.
[10] C. Wei, D. Gong, D. Xie, Y. Tang, The free-standing alloy strategy to improve the electrochemical performance of potassium-based dual-ion batteries, ACS Energy Lett. 6 (12) (2021) 4336–4344.
[11] Y. Zhu, X. Han, Y. Xu, Y. Liu, S. Zheng, K. Xu, L. Hu, C. Wang, Electrospun Sb/C fibers for a stable and fast sodium-ion battery anode, ACS Nano 7 (7) (2013) 6378–6386.
[12] Y.-Y. Hsieh, H.-Y. Tuan, Architectural van der Waals Bi_2S_3/Bi_2Se_3 topological heterostructure as a superior potassium-ion storage material, Energy Stor. Mater. 51 (2022) 789–805.
[13] D. Gong, C. Wei, D. Xie, Y. Tang, Ultrasmall antimony nanodots embedded in carbon nanowires with three-dimensional porous structure for high-performance potassium dual-ion batteries, Chem. Eng. J. 431 (2022) 133444.
[14] H. Kang, H. Kang, J. Piao, X. Xu, Y. Liu, S. Xiong, S. Lee, H. Kim, H.G. Jung, J. Kim, Relaxation of stress propagation in alloying-type Sn anodes for K-ion batteries, Small Methods 8 (1) (2024) 2301158.
[15] X. Huang, J. Sun, L. Wang, X. Tong, S. X. Dou, Z. M. Wang, Advanced high-performance potassium–chalcogen (S, Se, Te) batteries, Small 17 (6) (2021) 2004369.
[16] C.B. Chang, H.Y. Tuan, Recent progress on Sb-and bi-based chalcogenide anodes for potassium-ion batteries, Chem. Asian J. 17 (12) (2022) e202200170.
[17] Q. Pan, Z. Tong, Y. Su, Y. Zheng, L. Shang, Y. Tang, Flat–zigzag interface design of chalcogenide heterostructure toward ultralow volume expansion for high-performance potassium storage, Adv. Mater. 34 (39) (2022) 2203485.
[18] Z. Chen, Y. Zhao, F. Mo, Z. Huang, X. Li, D. Wang, G. Liang, Q. Yang, A. Chen, Q. Li, Metal-tellurium batteries: a rising energy storage system, Small Struct. 1 (2) (2020) 2000005.
[19] Y. Liu, J. Wang, Y. Xu, Y. Zhu, D. Bigio, C. Wang, Lithium–tellurium batteries based on tellurium/porous carbon composite, J. Mater. Chem. A 2 (31) (2014) 12201–12207.
[20] H. Liu, P. Wu, R. Wang, H. Meng, Y. Zhang, W. Bao, J. Li, A photo-rechargeable aqueous zinc–tellurium battery enabled by the Janus-jointed perovskite/Te photocathode, ACS Nano 17 (2) (2023) 1560–1569.
[21] Z. Chen, C. Li, Q. Yang, D. Wang, X. Li, Z. Huang, G. Liang, A. Chen, C. Zhi, Conversion-type nonmetal elemental tellurium anode with high utilization for mild/alkaline zinc batteries, Adv. Mater. 33 (51) (2021) 2105426.
[22] J. Zhou, D. Shen, X. Yu, B. Lu, Building ultra-stable K–Te battery by molecular regulation, J. Energy Chem. 69 (2022) 100–107.
[23] S. Dong, D. Yu, J. Yang, L. Jiang, J. Wang, L. Cheng, Y. Zhou, H. Yue, H. Wang, L. Guo, Tellurium: a high-volumetric-capacity potassium-ion battery electrode material, Adv. Mater. 32 (23) (2020) 1908027.
[24] W. Luo, D. Yu, J. Yang, H. Chen, J. Liang, L. Qin, Y. Huang, D. Chen, Regulating ion-solvent chemistry enables fast conversion reaction of tellurium electrode for potassium-ion storage, Chem. Eng. J. 473 (2023) 145312.
[25] D. Yu, W. Luo, H. Gu, K. Li, J. Liang, H. Chen, Q. Wang, D. Chen, Y. Huang, P. Novikov, Subnano-sized tellurium@ nitrogen/phosphorus co-doped carbon nanofibers as anode for potassium-based dual-ion batteries, Chem. Eng. J. 454 (2023) 139908.
[26] Q. Liu, W. Deng, C.-F. Sun, A potassium–tellurium battery, Energy Stor. Mater. 28 (2020) 10–16.
[27] H. Wang, Z. Tong, R. Yang, Z. Huang, D. Shen, T. Jiao, X. Cui, W. Zhang, Y. Jiang, C.S. Lee, Electrochemically stable sodium metal-tellurium/carbon nanorods batteries, Adv. Energy Mater. 9 (48) (2019) 1903046.
[28] Y. Zhang, W. Lu, P. Zhao, M.H.A. Shiraz, D. Manaig, D.J. Freschi, Y. Liu, J. Liu, A durable lithium–tellurium battery: effects of carbon pore structure and tellurium content, Carbon 173 (2021) 11–21.
[29] Y. Zhang, D. Manaig, D.J. Freschi, J. Liu, Materials design and fundamental understanding of tellurium-based electrochemistry for rechargeable batteries, Energy Stor. Mater. 40 (2021) 166–188.
[30] D. Yu, Q. Li, W. Zhang, S. Huang, Amorphous tellurium-embedded hierarchical porous carbon nanofibers as high-rate and long-life electrodes for potassium-ion batteries, Small 18 (32) (2022) 2202750.
[31] S. Yang, G.D. Park, Y.C. Kang, Conversion reaction mechanism of cobalt telluride-carbon composite microspheres synthesized by spray pyrolysis process for K-ion storage, Appl. Surf. Sci. 529 (2020) 147140.
[32] Y. Du, Z. Yi, Z. Zhang, J. Liao, Y. Xu, J. Bao, X. Zhou, A highly stable potassium-ion battery anode enabled by multilayer graphene sheets embedded with SnTe nanoparticles, Chem. Eng. J. 435 (2022) 135100.
[33] D.M. Soares, G. Singh, Superior electrochemical performance of layered WTe_2 as potassium-ion battery electrode, Nanotechnology 31 (45) (2020) 455406.
[34] H. Wu, G. Chan, J.W. Choi, I. Ryu, Y. Yao, M.T. McDowell, S.W. Lee, A. Jackson, Y. Yang, L. Hu, Stable cycling of double-walled silicon nanotube battery anodes through solid–electrolyte interphase control, Nat. Nanotechnol. 7 (5) (2012) 310–315.
[35] M.-H. Park, M.G. Kim, J. Joo, K. Kim, J. Kim, S. Ahn, Y. Cui, J. Cho, Silicon nanotube battery anodes, Nano Lett. 9 (11) (2009) 3844–3847.
[36] Z. Hu, J. Hao, D. Shen, C. Gao, Z. Liu, J. Zhao, B. Lu, Electro-spraying/spinning: a novel battery manufacturing technology, Green Energy Environ. 9 (1) (2024) 81–88.
[37] C. Zhang, Y. Xu, M. Zhou, L. Liang, H. Dong, M. Wu, Y. Yang, Y. Lei, Potassium Prussian blue nanoparticles: a low-cost cathode material for potassium-ion batteries, Adv. Funct. Mater. 27 (4) (2017) 1604307.

[38] H. Zhu, H. Zhang, J. Liang, G. Rao, J. Li, G. Liu, Z. Du, H. Fan, J. Luo, Controlled synthesis of tellurium nanostructures from nanotubes to nanorods and nanowires and their template applications, J. Phys. Chem. C 115 (14) (2011) 6375–6380.
[39] M. Shaijumon, S. Ramaprabhu, Synthesis of carbon nanotubes by pyrolysis of acetylene using alloy hydride materials as catalysts and their hydrogen adsorption studies, Chem. Phys. Lett. 374 (5–6) (2003) 513–520.
[40] J. Pandey, S. Mukherjee, D. Rawat, S. Athar, K.S. Rana, R.C. Mallik, A. Soni, Raman spectroscopy study of phonon liquid electron crystal in copper deficient superionic thermoelectric $Cu_{2-x}Te$, ACS Appl. Energy Mater. 3 (3) (2020) 2175–2181.
[41] C. Han, Z. Li, W.-j. Li, S.-l. Chou, S.-x. Dou, Controlled synthesis of copper telluride nanostructures for long-cycling anodes in lithium ion batteries, J. Mater. Chem. A 2 (30) (2014) 11683–11690.
[42] A. Ashok, A. Vasanth, T. Nagaura, M. Eguchi, N. Motta, H.P. Phan, N.T. Nguyen, J. G. Shapter, J. Na, Y. Yamauchi, Plasma-induced nanocrystalline domain engineering and surface passivation in mesoporous chalcogenide semiconductor thin films, Angew. Chem. Int. Ed. 61 (14) (2022) e202114729.
[43] S. Liu, N. Peng, Y. Bai, H. Xu, D. Ma, F. Ma, K. Xu, General solvothermal approach to synthesize telluride nanotubes for thermoelectric applications, Dalton Trans. 46 (13) (2017) 4174–4181.
[44] S. Ullah, G. Yasin, A. Ahmad, L. Qin, Q. Yuan, A.U. Khan, U.A. Khan, A.U. Rahman, Y. Slimani, Construction of well-designed 1D selenium–tellurium nanorods anchored on graphene sheets as a high storage capacity anode material for lithium-ion batteries, Inorg. Chem. Front. 7 (8) (2020) 1750–1761.
[45] V. Augustyn, J. Come, M.A. Lowe, J.W. Kim, P.-L. Taberna, S.H. Tolbert, H. D. Abruña, P. Simon, B. Dunn, High-rate electrochemical energy storage through Li^+ intercalation pseudocapacitance, Nat. Mater. 12 (6) (2013) 518–522.
[46] S. Ardizzone, G. Fregonara, S. Trasatti, "Inner" and "outer" active surface of RuO_2 electrodes, Electrochim. Acta 35 (1) (1990) 263–267.
[47] J. Wang, J. Polleux, J. Lim, B. Dunn, Pseudocapacitive contributions to electrochemical energy storage in TiO_2 (anatase) nanoparticles, J. Phys. Chem. C 111 (40) (2007) 14925–14931.
[48] W. Weppner, R.A. Huggins, Determination of the kinetic parameters of mixed-conducting electrodes and application to the system Li_3Sb, J. Electrochem. Soc. 124 (10) (1977) 1569.